Passivity-Based Design of External Passive Damper for *LCL*-Type Grid-Connected Inverter

Guangda Ma, *Student Member, IEEE*, Chuan Xie, *Senior Member, IEEE*, Cheng Li, *Student Member, IEEE*, Chao Peng, and Jianxiao Zou, *Member, IEEE*

***Abstract*—To enhance the interactive stability between an *LCL*-type grid-connected inverter (GCI) and the grid, a passive damper (PD) is necessary for passivizing the output admittance of the GCI system since an active damper (AD) may not work in scenarios such as beyond the Nyquist frequency. This article explores the best installation locations of PD where higher efficiency can be obtained. To this end, a general admittance model of *LCL*-type GCI with an internal PD (IPD) or external PD (EPD) for different scenarios is derived. By leveraging the derived model, the passivity compensation burden is compared for IPD and EPD by analyzing the amplification and reduction characteristics of output admittance seen from the point of common coupling (PCC). Then, the EPD additivity conditions are figured out for different scenarios to guide the installation of the PD in the GCI system, which can fulfill full-frequency passive output admittance at the expense of relatively lower damping losses. Moreover, a design method for the EPD is also detailed in the article. Finally, GCI prototypes with high or low switching frequencies are tested in the laboratory and compared with state-of-the-art PD methods. The experimental results verify the effectiveness and superiority of the proposed EPD method.**

***Index Terms*—Grid-connected inverter (GCI), passive damper (PD), passivity, stability.**

NOMENCLATURE

REN	Renewable energy.
GCI	Grid-connected inverter.
PD	Passive damper.
AD	Active damper.
HD	Hybrid damper.
CCF-AD	Capacitor-current-feedback AD.
CVF-AD	Capacitor-voltage-feedback AD.
PCC	Point of common coupling.
IPD	Internal PD.
EPD	External PD.
ICC	Inverter-side current control.
GCC	Grid-side current control.
PR	Proportional and resonant.
PLL	Phase-locked loop.
KCL	Kirchhoff Current Law.
EAC	EPD additivity conditions.
NP	Negative pole.
HSF	High-switching-frequency.
LSF	Low-switching-frequency.

I. INTRODUCTION

With the large-scale integration of the REN resources through *LCL*-type GCIs, the grid impedance becomes complex and variant [1], [2]. The variant grid impedance may push the interaction frequencies of the inverter-grid system into the nonpassive region of the output admittance of the GCI system. Then, the inverter-grid system will face risks of triggering oscillations either below or above the Nyquist frequency [3], [4].

The frequency-domain passivation technique for GCI's output admittance has emerged as a promising solution to tackle inverter-grid interactive instability [5]. By imposing a passive (nonnegative) real part in the output admittance, viz., $\mathrm{Real}\{Y(j\omega)\}\geq 0$ or $\angle Y(j\omega)\epsilon[-90^\circ, 90^\circ]\ \forall\omega$, it provides a sufficient stability condition for the GCIs operated in a wide-varied passive grid [6], [7]. In recent years, many research works have been devoted to the fields of passivity enhancement for GCIs. These methods can be roughly categorized into PD methods [8], [9], [10], AD methods [11], [12], [13], [14], [15], [16], and HD methods [17], [18], [19], [20].

The concept of the passivity theory can provide sufficient stability conditions for GCIs and is introduced to the PD design guideline in [8], which allows a relaxed design of the PD with reduced damping losses. In [9], the effect of the capacitance value of the *LCL*-filter on the output admittance of GCI is studied, and optimal capacitance value selection criteria for achieving passive output admittance is proposed. However, the passivity constraints applied in either [8] or [9] are limited to the Nyquist frequency, and conditions above the Nyquist frequency are not taken into account. To overcome this limitation, a general design guideline for RC-PD with passivity constraints extended above the Nyquist frequency is studied in [10]. Furthermore, a PD design procedure is proposed in [20] to provide the Pareto-optimal PD parameters with respect to full-frequency passivity

Manuscript received 8 December 2023; revised 27 February 2024 and 14 April 2024; accepted 13 May 2024. Date of publication 16 May 2024; date of current version 16 July 2024. This work was supported in part by the National Natural Science Foundation of China under Grant 51807021 and Grant 52107181, and in part by the Natural Science Foundation of SiChuan Province under Grant 2024NSFSC0118. Recommended for publication by Associate Editor A. Kuperman. *(Corresponding author: Chuan Xie.)*

Guangda Ma and Cheng Li are with the School of Automation Engineering, University of Electronic Science and Technology of China, Chengdu 611731, China (e-mail: gdma@std.uestc.edu.cn; chengli@std.uestc.edu.cn).

Chuan Xie, Chao Peng, and Jianxiao Zou are with the School of Automation Engineering and Shenzhen Institute for Advanced Study, University of Electronic Science and Technology of China, Chengdu 611731, China (e-mail: c.xie@uestc.edu.cn; pengchao@uestc.edu.cn; jxzou@uestc.edu.cn).

Color versions of one or more figures in this article are available at https://doi.org/10.1109/TPEL.2024.3402124.

Digital Object Identifier 10.1109/TPEL.2024.3402124

and efficiency. Although passivity-based design guidelines have enhanced the efficiency of PD and system stability robustness against variations in either *LCL* parameters or grid impedance [8], [21], the PD still suffers from the intrinsic defects of additional power loss and degradation in high-frequency attenuation capability of the *LCL*-filter [22].

Alternatives to completely cancel power loss in the PD are to simulate virtual resistors by feeding back state variables of the *LCL*-filter, also named AD methods [23]. The CCF-AD is a simple and effective way to achieve passive enhancement up to the Nyquist frequency [11], [12], [13], [14]. However, extra current sensors are required for the capacitor current feedback, which inevitably increases the cost [5]. To save sensors for AD, one alternative way is to estimate the capacitor current from its voltage by using a differentiator [15]. Nevertheless, there is still a nonpassive region of the output admittance near the Nyquist frequency due to the approximation accuracy degradation of the differentiator at the high-frequency range [24]. The observer-based AD method studied in [5] succeeds in saving sensors and achieving passive output admittance up to the Nyquist frequency. The CVF-AD can also help to enhance passivity and possess good dynamic performance [16]. The study in [12] indicates that the theoretical upper boundary of the nonnegative region for CVF-AD is one-third of the Nyquist frequency. Despite the merit of the high efficiency for AD, it suffers from the incapability of passivating the output admittance of GCIs above the Nyquist frequency due to the inherent characteristic of the digital control system [7], [10]. Besides, it also suffers from issues of increasing cost and implementation complexity [21].

By rationally combining the advantages of both PD and AD, HD methods can effectively balance their drawbacks to some extent [17], [18]. In the conventional HD design methods, the PD parameters are typically set to a critical minimum in the damping coefficient for the *LCL*-filter to obtain satisfactory efficiency, and AD is used only to improve the stability robustness against parameter variations in the GCI system [18]. However, passive output admittance for the GCI system has not been truly guaranteed. A passivity-based HD method is proposed in [19], where CCF-AD is designed to minimize the nonpassive region, and then PD is provided to enhance the passivity margin of the GCI system at the cost of relatively low damping losses. In [10], the passivity above the Nyquist frequency is taken into account in the HD design. However, one obvious weakness of HD is that it is too complex in design.

To further improve the efficiency of PD in reshaping the GCI's output admittance passive, this article investigates the effect of the installation location of the PD on its performance. Two scenarios are considered. The most common one is to install the PD branch inside of the *LCL*-filter, viz., parallel with the *LCL*-filter's capacitor, which is named the IPD. The other proposed one in this article is to install the PD branch outside of the *LCL*-filter, viz., at the PCC, which is called the EPD.

The rest of this article is organized as follows. In Section II, a general admittance model for *LCL*-type GCI with an IPD or EPD and its stability conditions are derived. In Section III, the passivity properties of the output admittance seen from the PCC are analyzed, and then the EPD additivity conditions (EACs) are figured out according to the PD's passivity compensation burden. The proposed EPD design procedure is elaborated in Section IV, and Section V validates the effectiveness and superiority of the proposed EPD method via experimental results. Finally, Section VI concludes this article.

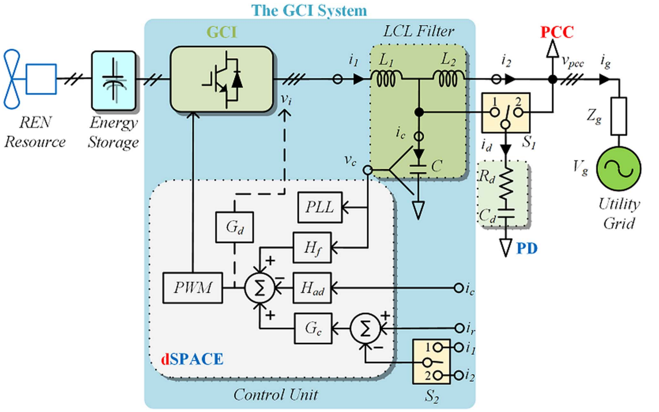

Fig. 1. General diagram of a three-phase and three-wire grounded *LCL*-type GCI system with an IPD or EPD.

II. Modeling of the *LCL*-Type GCI System With an IPD or EPD

A. System Description

Fig. 1 illustrates the general diagram of a three-phase and three-wire grounded *LCL*-type GCI system with an IPD or EPD. The power generated by the REN resource is stored in the dc-link capacitor. Then, the GCI provides the electricity output injected into the grid through the *LCL*-filter. In the filter components, L_1, L_2, and C represent the inverter-side inductor, the grid-side inductor, and the filter capacitor, respectively. In this article, the PD refers to a shunt RC branch that is installed in the GCI system through the selector S_1. When $S_1 = 1$, it is called IPD, which indicates the PD branch is internally parallel with the filter capacitor, while $S_1 = 2$ stands for EPD, which means that the PD is externally connected at the PCC. Note that the EPD has no impact on the high-frequency attenuation capacity of the *LCL*-filter. R_d and C_d are the damper resistor and capacitor of PD, respectively. Considering the worst-case scenario of the GCI system, this article ignores all parasitic resistors. For the grid side, Z_g represents the grid impedance and v_g is the grid voltage.

In the control unit, the control algorithm is executed in the $\alpha\beta$-frame to eliminate the complexities associated with decoupling terms for *LCL*-filter topology in the *dq*-frame [25]. The inverter-side current i_1 and the grid-side current i_2 are selectively fed back to the current controller G_c through the selector S_2, where $S_2 = 1$ represents the ICC mode and $S_2 = 2$ represents the GCC mode. In this article, G_c selects a PR controller to eliminate the steady-state tracking error of the reference current i_r [26], which can be expressed as

$$G_c = k_p + k_r \frac{\omega_b s}{s^2 + 2\omega_b s + \omega_0^2} \tag{1}$$

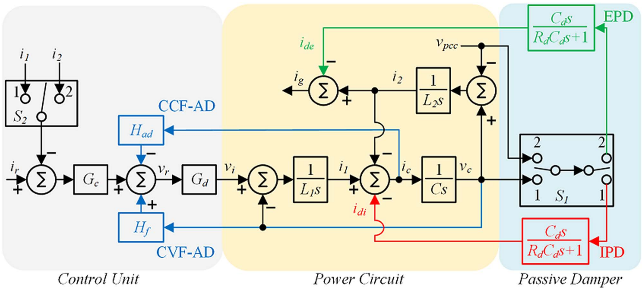

Fig. 2. Control diagram of the studied GCI system.

where k_p is the proportional gain, k_r is the resonator gain, ω_b is the bandwidth of the PR controller, and ω_0 is the fundamental angular frequency. During modeling and analyses of the output admittance, the PR controller is considered as a proportional gain k_p ($k_p = \omega_c L_1$, where ω_c is the crossover angular frequency). The reason is that the resonant part of the PR controller has almost negligible influence at frequencies above the fundamental frequency [11], [23]. Meanwhile, the capacitor voltage v_c is fed to the PLL to provide the grid synchronization signal [12] and to the CVF-AD controller H_f to suppress the current startup inrush [27]. The capacitor current i_c is fed to the CCF-AD controller H_{ad} to provide the virtual damping term. In addition, taking into consideration the one-sampling computation and pulsewidth modulation (considered as a zero-order holder) delay [3], the total delay link G_d is designated as

$$G_d = e^{-sT_s} \cdot \frac{1-e^{-sT_s}}{sT_s} = \gamma(\omega)\, e^{-sT_d} \tag{2}$$

where T_s is the sampling period and $\gamma(\omega) = \sin(0.5\omega T_s)/(0.5\omega T_s)$ is the gate function and $T_d = 1.5T_s$ is the total delay time. This article focuses on resonance below the sampling frequency since $\gamma(\omega)$ provides sufficient attenuation at high-frequency components.

B. Modeling of the Output Admittance

Fig. 2 shows a control diagram of the studied GCI system. As seen, the GCI's output voltage v_i can be expressed in the s-domain as

$$V_i = G_d \cdot \Big\{ \overbrace{G_c\left[I_r - (2-S_2)\, I_1 - (S_2-1)\, I_2\right] - H_{ad} I_c + H_f V_c}^{V_r} \Big\} \tag{3}$$

where v_r is the voltage reference. Note that uppercase symbols represent s-domain variables for their counterparts in the time domain in lowercase in this article.

According to the KCL, the grid-side current i_2 can be written as

$$I_2 = \overbrace{\frac{V_i - V_c}{L_1 s}}^{I_1} \overbrace{-CsV_c}^{I_c} - (2-S_1)\, \overbrace{Y_d V_c}^{I_{di}} \tag{4}$$

where i_{di} is the current drawn by the IPD, and Y_d is the admittance of the PD branch, with the form of

$$Y_d = \frac{C_d s}{C_d R_d s + 1}. \tag{5}$$

Substituting (3) into (4), with i_2 and v_c regarded as output and disturbance, respectively, yielding

$$I_2 = \overbrace{\frac{G_c G_d}{L_1 s + G_c G_d}}^{T_{ci}} \cdot I_r - \left\{ \overbrace{\frac{\left[\begin{array}{l} L_1 C s^2 + 1 + (2-S_2)\, G_c G_d C s \\ + H_{ad} G_d C s - H_f G_d \end{array}\right]}{L_1 s + G_c G_d}}^{Y_c} + (2-S_1) \cdot \overbrace{\frac{L_1 s + (2-S_2)\, G_c G_d}{L_1 s + G_c G_d} Y_d}^{Y_{di}} \right\} \cdot V_c \tag{6}$$

where T_{ci} is the internal closed-loop transfer function from i_r to i_2, Y_c is the output admittance as seen from v_c [12], and Y_{di} is the admittance of the IPD [10]. Note that if $S_2 = 1$, Y_{di} is equal to Y_d. Otherwise, Y_{di} is influenced by the controller. In addition, H_{ad} and H_f are respectively assigned as (7) for the passivity enhancement purpose [12]

$$\begin{cases} H_{ad} = \left(S_2 - 1 - \frac{36\omega_{r1}^2}{\omega_s^2}\right) \cdot G_c \\ H_f = K_f \left(1 - \alpha + \alpha e^{-sT_s}\right) \end{cases} \tag{7}$$

where ω_{r1} is the antiresonant angular frequency of L_1 and C, ω_s is the switching or sampling angular frequency, K_f is the gain for H_f, and α is the coefficient of the first-order finite-impulse response low-pass filter.

Following the KCL, the grid current i_g can be expressed as

$$I_g = \overbrace{(V_c - V_{pcc}) \cdot Y_{L2}}^{I_2} - (S_1 - 1)\, \overbrace{Y_d V_{pcc}}^{I_{de}} \tag{8}$$

where i_{de} is the current drawn by the EPD.

Substituting (8) into (6), and regarding i_g and v_{pcc} as output and disturbance, respectively, yielding

$$I_g = \overbrace{\frac{T_{ci} Y_{L2}}{Y_{L2} + Y_c + (2-S_1) \cdot Y_{di}}}^{T_{cg}} \cdot I_r - \left\{ \underbrace{\overbrace{\frac{\left[Y_c + (2-S_1) \cdot Y_{di}\right] Y_{L2}}{Y_{L2} + Y_c + (2-S_1) \cdot Y_{di}}}^{Y_{\text{pcc}}} + (S_1 - 1)\, Y_d}_{Y_{\text{pcc}d}} \right\} \cdot V_{\text{pcc}} \tag{9}$$

where T_{cg} is the internal closed-loop transfer function from i_r to i_g, and Y_{pcc} and $Y_{\text{pcc}\,d}$ are the output admittance as seen from the PCC without and with the embedded PD branch, respectively. Then, the equivalent circuit of the studied GCI system can be obtained, as shown in Fig. 3.

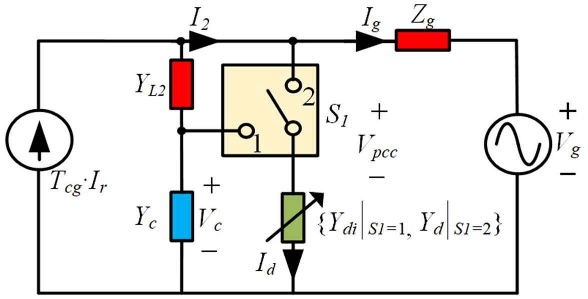

Fig. 3. Equivalent circuit for *LCL*-type GCI system with an IPD or EPD.

C. Overall Closed-Loop System Stability Condition Analysis

Combined (9) with $V_g = V_{\text{pcc}} + I_g \cdot Z_g$, the overall closed-loop current response can be derived as

$$I_g = \overbrace{\{T_{cg} I_r - Y_{\text{pcc}d} V_g\}}^{\text{First item}} \cdot \overbrace{\frac{1}{1 + Z_g \cdot Y_{\text{pcc}d}}}^{\text{Second item}}. \tag{10}$$

From (10), the stability of the first item is independent of the grid impedance Z_g, which requires the GCI system to be stabilized internally by itself. Meanwhile, the stability of the second item is related to Z_g, which is defined by external stability [1]. According to the frequency-domain passivity theory [24], the inverter-grid system is interactively stable if the following two conditions hold [8].

1) Internal stability condition: T_{cg} is asymptotically stable.

2) External stability condition: Both Z_g and $Y_{\text{pcc}\,d}$ are passive.

As seen in Fig. 3, if the IPD is used and $S_1 = 1$, T_{cg} and $Y_{\text{pcc}\,d}$ can be rewritten as

$$\begin{cases} T_{cg}\,|_{S_1=1} = T_{ci} \cdot \frac{1}{1+(Y_c+Y_{di})/Y_{L2}} \\ Y_{\text{pcc}d}\,|_{S_1=1} = \frac{1}{1/Y_{L2}+1/(Y_c+Y_{di})} \end{cases}. \tag{11}$$

Since T_{ci} is a first-order system with purely delayed elements, it can be easily stabilized [12]. As L_2 is a passive component, a sufficient stability condition for T_{cg} and $Y_{\text{pcc}\,d}$ can be achieved when Y_{di} reshapes Y_c to be the full-frequency passive, viz., the following inequality holds:

$$\operatorname{Re}\{Y_c(j\omega)\} + \operatorname{Re}\{Y_{di}(j\omega)\} \geq 0 \forall \omega \leq \omega_s. \tag{12}$$

Alternatively, if the EPD is put into operation and $S_1 = 2$, T_{cg} and $Y_{\text{pcc}\,d}$ are rewritten as

$$\begin{cases} T_{cg}\,|_{S_1=2} = T_{ci} \cdot \frac{1}{1+Y_c/Y_{L2}} \\ Y_{pccd}\,|_{S_1=2} = \overbrace{\frac{Y_c \cdot Y_{L2}}{Y_c + Y_{L2}}}^{Y_{pcc}} + Y_d \end{cases}. \tag{13}$$

Looking into (13), its stability condition for T_{cg} can be met when the inherent resonant frequency of the *LCL*-filter ω_r is located in the passive regions of Y_c. It imposes constraints on the parameter design of the *LCL*-filter [26].

$$\omega_r = \sqrt{\frac{L_1 + L_2}{L_1 L_2 C}} \tag{14}$$

For the external stability condition, the remaining is to make $Y_{\text{pcc}\,d}$ passive, viz., the following inequality holds:

$$\operatorname{Re}\{Y_{pcc}(j\omega)\} + \operatorname{Re}\{Y_d(j\omega)\} \geq 0 \forall \omega \leq \omega_s. \tag{15}$$

III. DISCUSSIONS ON SELECTION OF IPD OR EPD

Looking into (12) and (15), it implies that the passivity compensation constraints for IPD and EPD are related to the passivity properties of Y_c and Y_{pcc}, respectively. In this section, the passivity compensation burdens are compared for IPD and EPD in terms of analyzing the magnitude variation of real parts of Y_c and Y_{pcc}. Then, the EACs are figured out.

A. Analysis of Magnitudes of Real Parts of $\mathrm{Y_c}$ *and* Y_{pcc}

According to (9), taking the real part of Y_{pcc} with $S_1 = 2$ yields

$$\begin{cases} \operatorname{Re}\{Y_{pcc}(j\omega)\} = \frac{\operatorname{Re}\{Y_c(j\omega)\}}{\rho(\omega)} \\ \rho(\omega) = \left(\frac{\operatorname{Re}\{Y_c(j\omega)\}}{\operatorname{Im}\{Y_{L2}(j\omega)\}}\right)^2 + \left(\frac{\operatorname{Im}\{Y_c(j\omega)\}}{\operatorname{Im}\{Y_{L2}(j\omega)\}} + 1\right)^2 \\ \operatorname{Re}\{Y_c(j\omega)\} \\ \quad = \frac{\left\{\begin{bmatrix} L_1 C\left(\omega_{r1}^2 - \omega^2\right)(S_2 - 1) \\ +(2 - S_2) + H_{ad}\frac{C\omega^2}{\omega_c} \end{bmatrix} \cdot \gamma(\omega)\,\omega_c \cos(\omega T_d) \atop +H_f \gamma^2(\omega)\,\omega_c - H_f \gamma(\omega)\,\omega_c \sin(\omega T_d)\right\}}{L_1[\omega^2 + \gamma^2(\omega)\omega_c^2 - 2\gamma(\omega)\omega_c \omega \sin(\omega T_d)]} \end{cases} \tag{16}$$

where $\rho(\omega)$ is a proportional factor between real parts of Y_c and Y_{pcc}. Re$\{Y_c(\text{j}\omega)\}$ and Im$\{Y_c(\text{j}\omega)\}$ are the real and imaginary parts of Y_c, respectively. Im$\{Y_{L2}(\text{j}\omega)\}$ is the imaginary part of Y_{L2}. Since the value of $\rho(\omega)$ is always nonnegative over the entire frequency range, it will not change the polarity between Re$\{Y_{\text{pcc}}(\text{j}\omega)\}$ and Re$\{Y_c(\text{j}\omega)$, but will change the magnitude and lead to different passivity compensation burdens. It can be easily inferred that if $\rho(\omega) < 1$, from Y_c to Y_{pcc}, the magnitude of the real part will be amplified. Otherwise, if $\rho(\omega) > 1$, the magnitude of the real part will be reduced. However, the separation points of the amplifying and reducing regions are difficult to calculate directly from (16).

According to (6), Y_c can be rewritten as

$$Y_c = \frac{1 - T_{ci}}{L_1 s} + Cs \cdot [2 - S_2 + (S_2 - 1) \cdot (1 - T_{ci})]$$
$$+ \left[\left(1 - \frac{36\omega_{r1}^2}{\omega_s^2}\right) Cs - \frac{K_f}{G_c}\right] \cdot T_{ci}. \tag{17}$$

T_{ci} possesses low pass filter characteristics. When ω_c is designed to be sufficiently small (ω_c is typically recommended to be less than $\omega_s/10$ [28]), T_{ci} can be simplified as 0 at the high-frequency range. Then, Y_c can be approximated as

$$Y_c \approx \frac{1}{L_1 s} + Cs = Y_{c,\text{app}} \tag{18}$$

where $Y_{c,\text{app}}$ is the approximation admittance for Y_c.

Taking the real and imaginary parts of $Y_{c,\text{app}}$ gives

$$\operatorname{Re}\{Y_{c,app}(j\omega)\} = 0 \text{ and } \operatorname{Im}\{Y_{c,app}(j\omega)\} = C\omega - \frac{1}{L_1 \omega}. \tag{19}$$

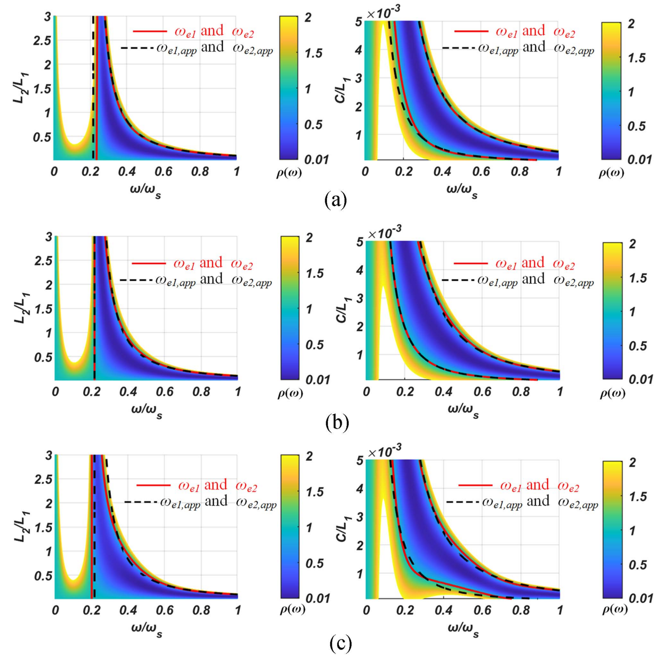

Fig. 4. Top views of 3D plots of $\rho(\omega)$ along with variations of inductance and capacitance of the *LCL*-filter for (a) single-loop ICC, (b) single-loop GCC, and (c) ICC or GCC with AD (C is set to 10 μF when the ratio of L_2 to L_1 changes, and L_2 is set to 3 mH when the ratio of C to L_1 varies).

Substituting (19) into (16), $\rho(\omega)$ can be simplified as

$$\begin{aligned}\rho_{\text{app}}(\omega) &= \left(\frac{\operatorname{Im}\{Y_{c,\text{app}}(j\omega)\}}{\operatorname{Im}\{Y_{L2}(j\omega)\}}+1\right)^2 \\ &= \left(\frac{L_1+L_2}{L_1}-L_2C\omega^2\right)^2 \end{aligned} \tag{20}$$

where $\rho_{\text{app}}(\omega)$ is the approximation proportional factor for $\rho(\omega)$. Then, the amplifying and reducing regions for $\rho_{\text{app}}(\omega)$ can be analytically separated as

$$\begin{cases} \text{Amplifying Region}(\rho_{\text{app}}(\omega)<1): \omega_{e1,\text{app}}<\omega<\omega_{e2,\text{app}} \\ \text{Reducing Region}(\rho_{\text{app}}(\omega)>1): \begin{matrix} 0<\omega<\omega_{e1,\text{app}} \\ \text{or} \quad \omega>\omega_{e2,\text{app}} \end{matrix} \end{cases} \tag{21}$$

where $\omega_{e1,\text{app}} = \frac{1}{\sqrt{L_1 C}}$ and $\omega_{e2,\text{app}} = \sqrt{\frac{2L_1+L_2}{L_1 L_2 C}}$.

Fig. 4 shows top views of three-dimensional (3-D) plots of $\rho(\omega)$ along with variations of inductance and capacitance of the *LCL*-filter for different scenarios of single-loop ICC, single-loop GCC, and ICC or GCC with AD. It can be seen that the separation lines of amplifying and reducing regions determined by analytical values, i.e., $\omega_{e1,\text{app}}$ and $\omega_{e2,\text{app}}$, almost overlap with the numerical ones (denoted by ω_{e1} and ω_{e2}) that directly obtained from (16). Although a bias still exists between the analytical separation line and the numerical one that stands for the real one, the bias is sufficiently small and acceptable for engineering design. For the sake of simplicity, only ω_{e1} and ω_{e2} are used to represent the boundaries of amplifying and reducing regions in the rest of this article.

TABLE I
EPD ADDITIVITY CONDITIONS FOR DIFFERENT SCENARIOS

Scenarios	Constraints
ICC	$\omega_c < \omega_{e1} < \omega_{e2} < \omega_s/6$ or $\omega_s/2 < \omega_{e1} < \omega_{e2} < 5\omega_s/6$
GCC	$\omega_s/6 < \omega_{e1} < \omega_{e2} < \omega_s/2$ or $5\omega_s/6 < \omega_{e1} < \omega_{e2} < \omega_s$
With AD	$\omega_c < \omega_{e1} < \omega_{e2} < \omega_s/2$ or $5\omega_s/6 < \omega_{e1} < \omega_{e2} < \omega_s$

As mentioned above, $\rho(\omega)$ is only a proportional factor between real parts of Y_c and Y_{pcc}. It does not change their polarity. That is to say, when the nonpassive regions are all included in the reducing regions, the passivity compensation burden on Y_{pcc} will be more relaxed compared to that on Y_c. In consequence, incorporating EPD will have higher efficiency in compensating nonpassive regions of the output admittance. Conversely, if the nonpassive region is located in the amplifying region, the passivity compensation burden on Y_{pcc} will be increased, and installing the IPD will be more advisable. In the next subsection, the EACs for different scenarios will be further figured out.

B. EPD Additivity Conditions for Different Scenarios

Incorporating with the passivity properties of Y_c that have been well reported in previous work [10], the EACs can be easily figured out by checking whether the nonpassive regions in Y_c are located in reducing regions defined by (21).

1) *Single-Loop ICC ($S_2 = 1$)*: The nonpassive regions of Y_c are $[\omega_s/6, \omega_s/2]$ and $[5\omega_s/6, \omega_s]$. Assign the nonpassive regions of Y_c in the reducing regions of $\rho(\omega)$, the EAC for the single-loop ICC can be derived as

$$\begin{cases} \frac{\omega_{e1}}{\omega_s} \geq 0.5k-0.5 \\ \frac{\omega_{e2}}{\omega_s} \leq 0.5k-\frac{3-(-1)^k}{12} \end{cases}, k=1 \text{or} k=2. \tag{22}$$

2) *Single-Loop GCC ($S_2 = 2$):* The nonpassive regions of Y_c are not only dependent on the time delay, but also affected by ω_{r1} [12]. When $\omega < \omega_{r1}$, the polarity of $\operatorname{Re}\{Y_c(j\omega)\}$ at $S_2 = 2$ is the same as that of $\operatorname{Re}\{Y_c(j\omega)\}$ at $S_2 = 1$, and it is precisely opposite when $\omega > \omega_{r1}$. Assigning the nonpassive regions of Y_c in the reducing regions of $\rho(\omega)$, the EAC for single-loop GCC can be derived as

$$\begin{cases} \frac{\omega_{e1}}{\omega_s} \geq 0.5k-\frac{3-(-1)^k}{12} \\ \frac{\omega_{e2}}{\omega_s} \leq 0.5k \end{cases}, k=1 \text{or} k=2. \tag{23}$$

3) *ICC or GCC With AD:* The nonpassive region of Y_c is $[\omega_s/2, 5\omega_s/6]$, and thus assign the nonpassive regions of Y_c in the reducing regions of $\rho(\omega)$, the EAC for the ICC or GCC with AD can be derived as

$$\omega_{e2} \leq 0.5\omega_s \text{or} \begin{cases} \omega_{e1} \geq \frac{5}{6}\omega_s \\ \omega_{e2} \leq \omega_s \end{cases}. \tag{24}$$

The EACs for different scenarios are given in Table I. If the EACs are satisfied, EPD is recommended due to the lighter passivity compensation burden. Otherwise, IPD is more advisable. Note that EACs also imply that the internal stability condition of (13) is satisfied since ω_r is smaller than ω_{e2} and thus is located in the passive regions of Y_c.

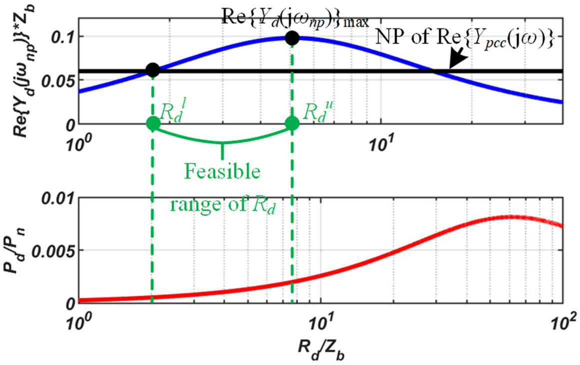

Fig. 5. Diagram of passivity and damping losses of the EPD with the variation of R_d ($\omega_{np} = 0.2\omega_s$), where the blue solid line represents $\mathrm{Re}\{Y_d(j\omega_{np})\}$, the black solid line represents NP of $\mathrm{Re}\{Y_{\mathrm{pcc}}(j\omega)\}$, and the red solid line represents P_d.

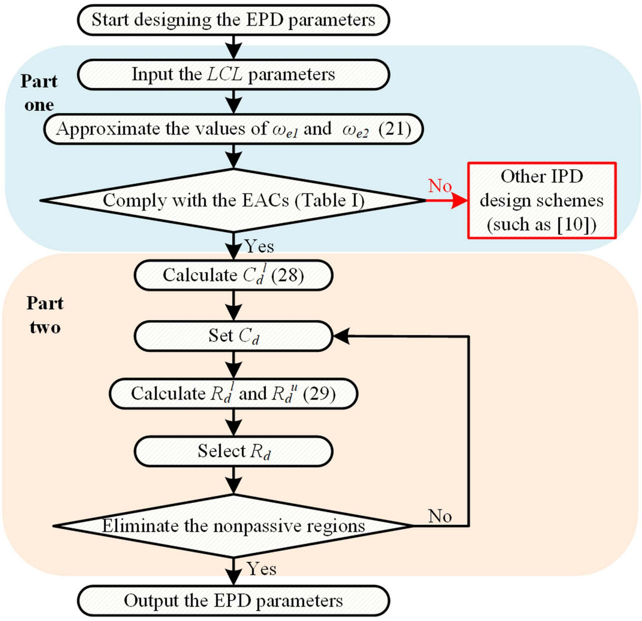

Fig. 6. Flowchart of the proposed EPD design method.

TABLE II
PROTOTYPE PARAMETERS

Symbol		Description	Value (p.u.)	Value (p.u.)
Power Stage	P_n	Rated power	1.4 kW (1)	1.4 kW (1)
	V_{dc}	Input DC voltage	350 V (3.18)	350 V (3.18)
	V_g	Grid phase voltage	110 V (1)	110 V (1)
	f_0	Grid frequency	50 Hz (1)	50 Hz (1)
	L_1	Inverter-side inductor	2.0 mH (0.02)	6.0 mH (0.07)
	L_2	Grid-side inductor	3.0 mH (0.04)	4.0 mH (0.05)
	C	Filter capacitor	15.0 μF (0.12)	15.0 μF (0.12)
Controller	f_s	Sampling freq.	10 kHz (200)	3 kHz (60)
	K_p	Proportional gain	6.8 Ω	6.1 Ω
	K_I	Integral gain	2322.4 Ω/s	634.2 Ω/s
	ω_c	Crossover freq.	3406rad/s (0.05)	1022 rad/s (0.05)

TABLE III
PARAMETERS AND DAMPING LOSSES OF EPD

	Symbol	Case I	Case II	Case III
Theoretical Values	C_d	0.14 μF (0.0011)	0.79 μF (0.0064)	0.09 μF (0.0007)
	R_d	468.2 Ω (18.06)	60.0 Ω (2.31)	700.5 Ω (27.02)
	Feasible range of R_d	277.1 Ω (10.69) ~ 659.3 Ω (25.43)	2.4 Ω (0.09) ~ 117.6 Ω (4.54)	296.1 Ω (11.42) ~ 1104.9 Ω (42.61)
Experimental Values	C_d	3.5 μF (0.03)	3.5 μF (0.03)	3.5 μF (0.03)
	R_d	0.7 Ω (0.03)	3.0 Ω (0.12)	0.3 Ω (0.01)
	Feasible range of R_d	0.36 Ω (0.014) ~ 25.81 Ω (0.995)	0.12 Ω (0.005) ~ 26.46 Ω (1.021)	0.16 Ω (0.006) ~ 26.28 Ω (1.014)
Damping Losses	P_d	0.03 W (2.25×10^{-5})	0.13 W (9.52×10^{-5})	0.02 W (1.24×10^{-5})

IV. DESIGN METHOD FOR THE PROPOSED EPD

To make the EPD scheme for the EAC-compliant GCI system as cost-effective and highly efficient as possible, the characteristics of passivity and damping losses of the EPD are analyzed first, and then the EPD design procedure is put forward.

A. Characteristics of Passivity and Damping Losses of the EPD

Substituting $s = j\omega$ into (5) and taking the real part of Y_d yields

$$\mathrm{Re}\left\{Y_d\left(j\omega\right)\right\} = \frac{\omega^2 C_d^2 R_d}{1 + \omega^2 C_d^2 R_d^2}. \tag{25}$$

Looking into (25), the sign of $\mathrm{Re}\{Y_d(j\omega)\}$ is positive in the entire frequency range so that the installation of EPD can provide a strong passive enhancement. Moreover, the magnitude of $\mathrm{Re}\{Y_d(j\omega)\}$ is a monotonic increasing function of C_d and a second-order function of R_d. As a result, there is a maximum value as follows:

$$\mathrm{Re}\{Y_d\left(j\omega\right)\}_{\max} = \mathrm{Re}\left\{Y_d\left(j\omega\right)\right\}\big|_{R_d = 1/(\omega C_d)} = \frac{\omega C_d}{2}. \tag{26}$$

From (26), the maximum values of $\mathrm{Re}\{Y_d(j\omega)\}$ for different frequencies are achieved when R_d is equivalent to $1/(\omega C_d)$. Assuming that the NP in $\mathrm{Re}\{Y_{\mathrm{pcc}}(j\omega)\}$ is aligned to the maximum value of $\mathrm{Re}\{Y_d(j\omega)\}$, then the EPD can provide maximum passive enhancement.

For the GCI system, the total harmonic distortion of current is limited to below 5% [29], and thus, the main component in grid-side currents is the fundamental current. That is, the dominant damping losses in the EPD are produced by the fundamental current. Then, the expression of the damping losses in the per-unit (p.u.) can be given as

$$P_d^* = \frac{P_d}{P_n} = \frac{\mathrm{Re}\left\{Y_d\left(j\omega_o\right)\right\} \cdot V_{pcc}^2}{V_{pcc}^2 / Z_b} = Z_b \cdot \mathrm{Re}\left\{Y_d\left(j\omega_o\right)\right\} \tag{27}$$

TABLE IV
THEORETICAL VALUES OF OTHER STATE-OF-ART IPD METHODS

	Symbol	Case I	Case II	Case III
Wu et al. [31]	C_d	-	1.05 μF (0.0086)	-
	R_d	-	186.92 Ω (7.21)	-
Beres et al. [32]	C_d	1.05 μF (0.0086)	1.05 μF (0.0086)	-
	R_d	136.76 Ω (5.27)	193.41Ω (7.46)	-
Solatialkaran et al. [33]	C_d	1.05 μF (0.0086)	1.05 μF (0.0086)	-
	R_d	136.76 Ω (5.27)	193.41Ω (7.46)	-
Liu et al. [17]	C_d	-	-	1.05 μF (0.0086)
	R_d	-	-	190.13 Ω (7.33)
Zhao et al. [9]	C_d	-	1.89 μF (0.0154)	-
	R_d	-	30.17 Ω (1.16)	-
Liu et al. [19]	C_d	-	-	-
	R_d	-	-	0.22 Ω (0.01)
Ma et al. [10]	C_d	1.06 μF (0.0086)	1.20 μF (0.0098)	1.26 μF (0.0100)
	R_d	53.70 Ω (2.07)	56.00 Ω (2.16)	48.60 Ω (1.87)
Ma et al. [20]	C_d	5.81 μF (0.0473)	18.4 μF (0.1499)	3.89 μF (0.0316)
	R_d	1.92 Ω (0.07)	0.29 Ω (0.01)	5.60 Ω (0.22)

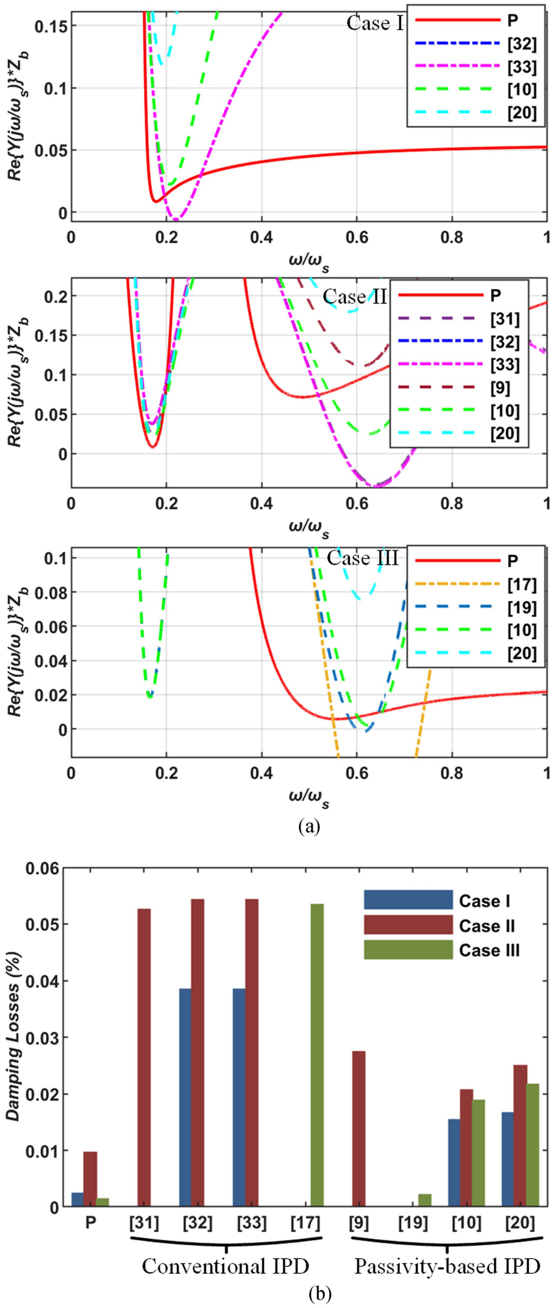

(a)

(b)

Fig. 7. (a) Plots of the real part of the output admittance for different methods and (b) bar graph of damping losses from different methods (*P* is the proposed method).

where $V_{\rm pcc}$ is the nominal value of PCC voltage and Z_b is the base impedance.

Comparing (27) with (25), in the p.u., the value of P_d^* is in line with the magnitude of $\text{Re}\{Y_d(\text{j}\omega)\}\cdot Z_b$ if ω takes ω_0. In practical implementation, the angular frequency ω_{np} of NP is much greater than ω_0. This means that (25) can be regarded as a monotonically increasing function of R_d and C_d, as shown in Fig. 5. While ensuring that the output admittance is enhanced to be passive at all frequencies, small values of R_d and C_d will greatly reduce the negative impact of the EPD on efficiency. Note that a small value of R_d will result in a small passivity margin against *LCL* parameters fluctuation.

B. Proposed EPD Design Method

Fig. 6 gives the flowchart of the proposed EPD design procedure, which includes the following two parts.

Part one (EACs Checking): Input the *LCL* parameters into (21) to approximate the values of ω_{e1} and ω_{e2}. Based on Table I, check whether the target system agrees with the EACs.

Part two (EPD Parameters Selection): If the target system agrees with the EACs, the EPD scheme can be implemented. Otherwise, switch to other IPD design schemes. The EPD parameter design includes the following four steps.

1) Based on (26), calculate the lower boundary of C_d to

$$C_d^l = \frac{2\left|\text{Re}\left\{Y_{pcc}\left(j\omega_{np}\right)\right\}\right|}{\omega_{np}} \tag{28}$$

where C_d^l represents the lower boundary of C_d.

2) Set the initial value of C_d according to (28). Based on (25) and (26), the lower and upper boundaries of R_d are calculated as

$$\begin{cases} R_d^l = \frac{\omega_{np}C_d - \sqrt{(\omega_{np}C_d)^2 - 4(|\text{Re}\{Y_{pcc}(j\omega_{np})\}|)^2}}{2|\text{Re}\{Y_{pcc}(j\omega_{np})\}|\omega_{np}C_d} \\ R_d^u = \frac{1}{\omega_{np}C_d} \end{cases} \tag{29}$$

where R_d^l is the lower boundary of R_d and R_d^u is the upper boundary of R_d.

3) Select the initial value of R_d based on (29). For reduced damping losses, a small value of R_d should be selected. Similarly, a large value of R_d should be chosen if a sufficient passivity margin is emphasized in practical implementation.

4) Verify the passivity of the output admittance. If the nonpassive regions still exist, then go back to 2) and update the value of C_d to a larger value.

V. SIMULATION AND EXPERIMENTAL VERIFICATION

To verify the feasibility of the EACs in different scenarios, power stage parameters suitable for GCI systems with either HSF or LSF are designed following the guidelines in [30], and results are given in Table II. Moreover, their corresponding

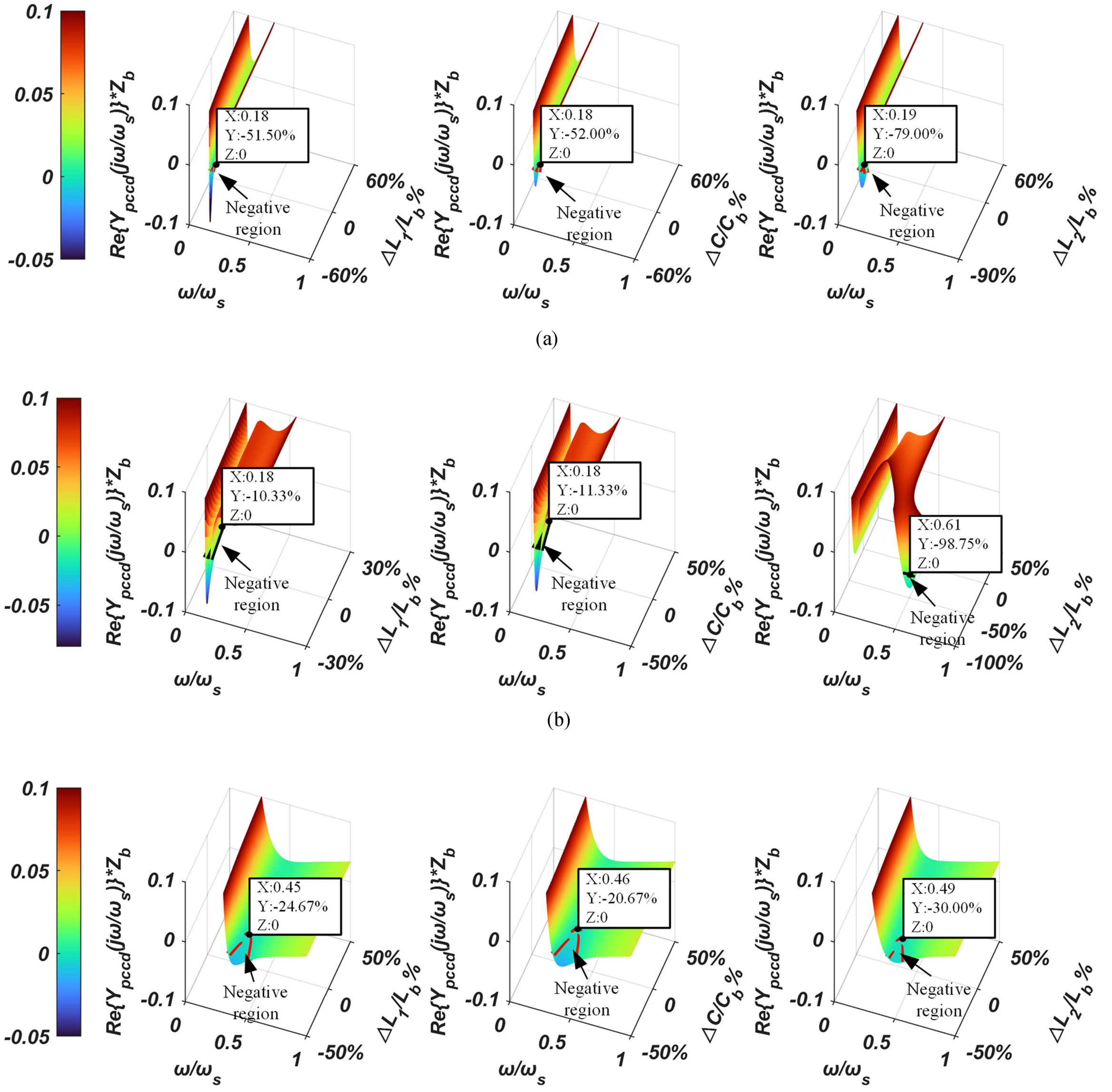

(a)

(b)

(c)

Fig. 8. 3-D plots of the real part of the output admittance with the proposed EPD in the presence of *LCL* parameters variations for the three cases. (a) Case I. (b) Case II, or (c) case III.

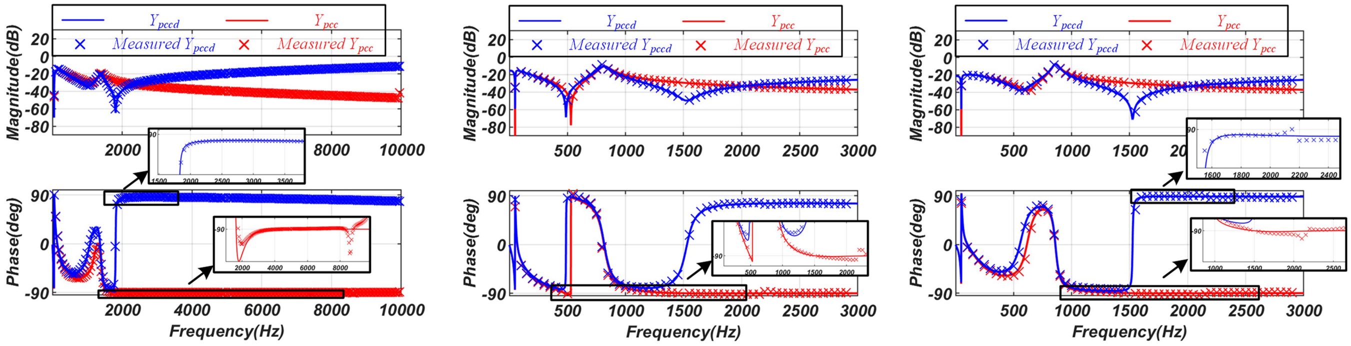

(a)

(b)

(c)

Fig. 9. Comparison of output admittance of the GCI system. (a) Case I. (b) Case II. (c) Case III.

Fig. 10. Hardware Photograph for the experimental setup.

controller parameters are designed according to [12], and results are also given in Table II.

A. EACs Checking and EPD Results Analysis

According to (21), the approximate values for ω_{e1} and ω_{e2} are 0.09 p.u. and 0.14 p.u. for the HSF-GCI system and 0.18 and 0.35 p.u. for the LSF-GCI system, respectively. Referring to Table I, the HSF-GCI system complies with the EACs in ICC, while the LSF-GCI system agrees with the EACs in GCC, and both systems meet the EACs with AD.

With the EPD design method proposed in Section IV-B, the theoretical design results of the EPD parameters are listed in Table III for three different cases, i.e., case I: HSF-GCI system in single-loop ICC, case II: LSF-GCI system in single-loop GCC, and Case III: LSF-GCI system in GCC with CCF- and CVF-ADs (H_{ad}, α, and H_f are set to -0.77, 0.5 and 0.5, respectively.). The theoretical value of the damping losses is calculated from (27) and given in Table III. Considering commercial accessibility, experimental parameters of EPD are re-set and share the same theoretical damping losses, and results are also given in Table III.

To emphasize the advantages of the proposed EPD method, comparisons with the other state-of-the-art IPD methods (conventional IPD methods [17], [31], [32], [33] and passivity-based IPD methods [9], [10], [19], [20]) are performed for three cases. The parameters of these IPD methods are given in Table IV. Looking at the theoretical values of Table III and that of Table IV, it is clearer that the proposed EPD method can provide smaller values of C_d and R_d, which indicate higher efficiency for case II. First, it can be found from Fig. 7(a) that the proposed EPD method is feasible in eliminating the nonpassive regions of the output admittance at full frequency in all cases, whereas the conventional IPD methods and method in [19] cannot always ensure the full-frequency passive output admittance. This is because the wide variation of grid impedance or the risk of oscillations above the Nyquist frequency is outside the consideration of the design guidelines of these methods.

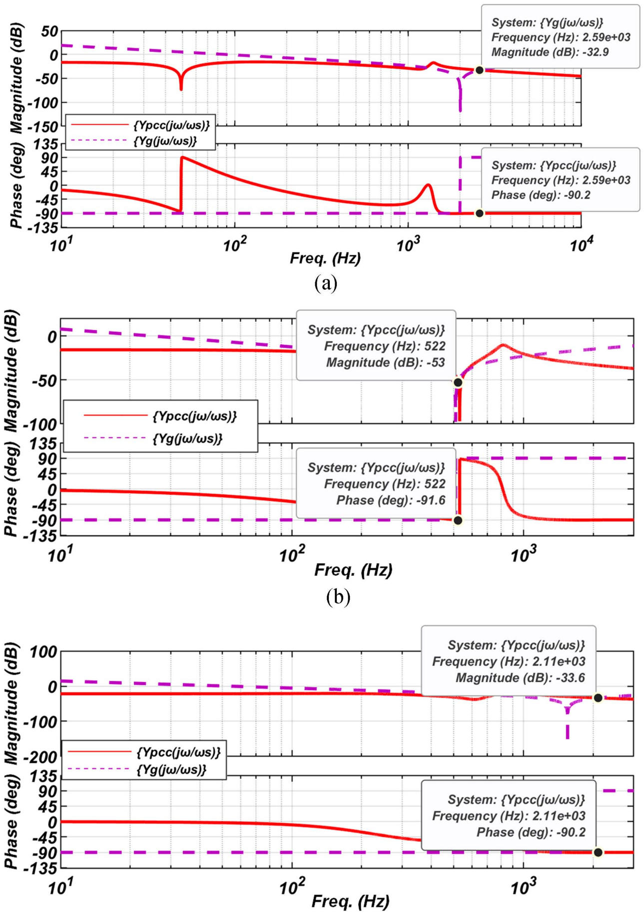

(c)

Fig. 11. Bode diagrams of Y_{pcc} and Y_g (a) for case I where the value of L_g is 0.02 p.u. and the value of C_g is 0.03 p.u., (b) for case II where the value of L_g is 0.08 p.u. and the value of C_g is 0.12 p.u., (c) for case III where the value of L_g is 0.04 p.u. and the value of C_g is 0.03 p.u.

As shown in Fig. 7(b), passivity-based IPD methods are more efficient than conventional IPD methods due to more relaxed design guidelines, yet they are inferior to the proposed EPD method in efficiency for the GCI system when EACs are satisfied. The proposed EPD method yields the lowest damping losses among these methods in all cases. Further, the damping losses in case II are relatively high compared to the other two cases, which is due to the LSF characteristics leading to relatively large parameters for EPD. This issue can be significantly mitigated by introducing AD to push the nonpassive region of Y_{pcc} into the high-frequency range. Case III exactly confirms this expectation.

Since the EPD is installed in the PCC, it does not degrade the high-frequency attenuation capability of the *LCL*-filter compared to these IPDs.

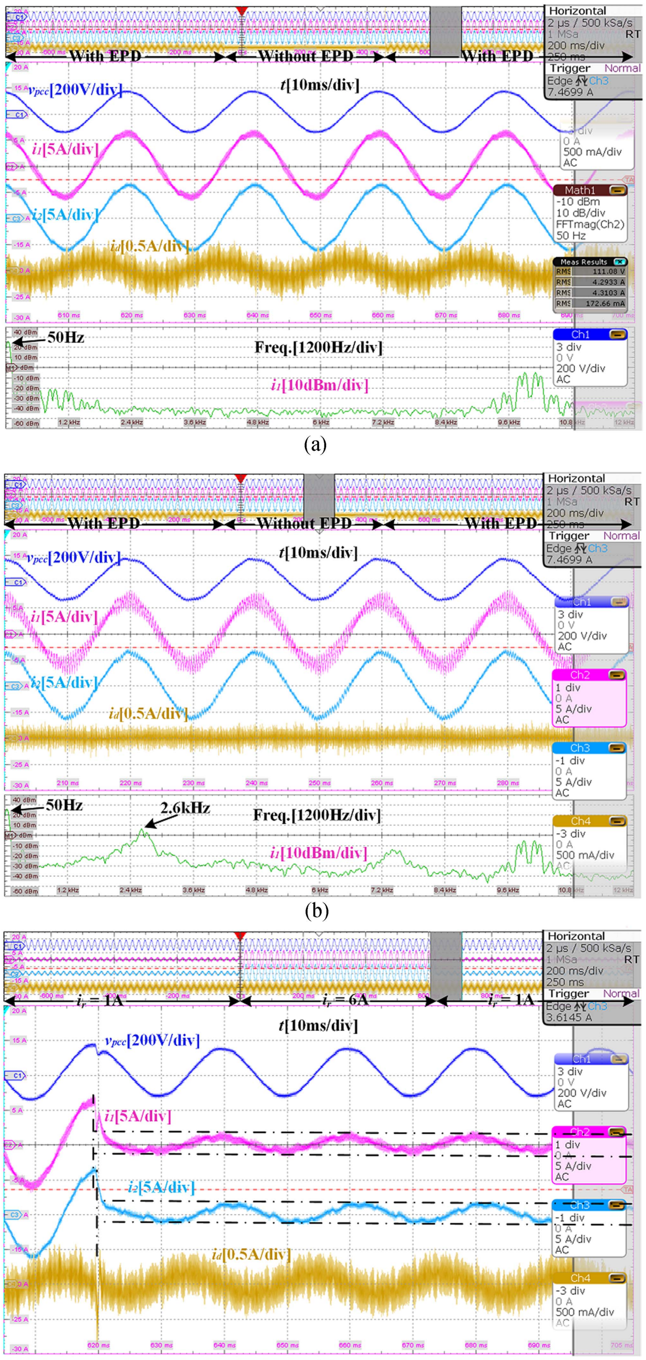

(a)

(b)

(c)

Fig. 12. Experimental waveforms for case I (a) with or (b) without the EPD. (c) Step change of reference current from 6 to 1 A.

The influence of variations in power circuit parameters on the passivity of the GCI system with the EPD is graphically analyzed. Fig. 8 gives the real part of the output admittance with the proposed EPD in the presence of *LCL* parameters' variations for the three cases. The full-frequency passive output admittance can be maintained for the three cases if tolerances for L_1, L_2 and C of the *LCL*-filter are less than 51.5%, 52% and 79% for case I, 10.33%, 11.33%, and 98.75% for case II, 24.67%, 20.67%, and 30% for case III, respectively.

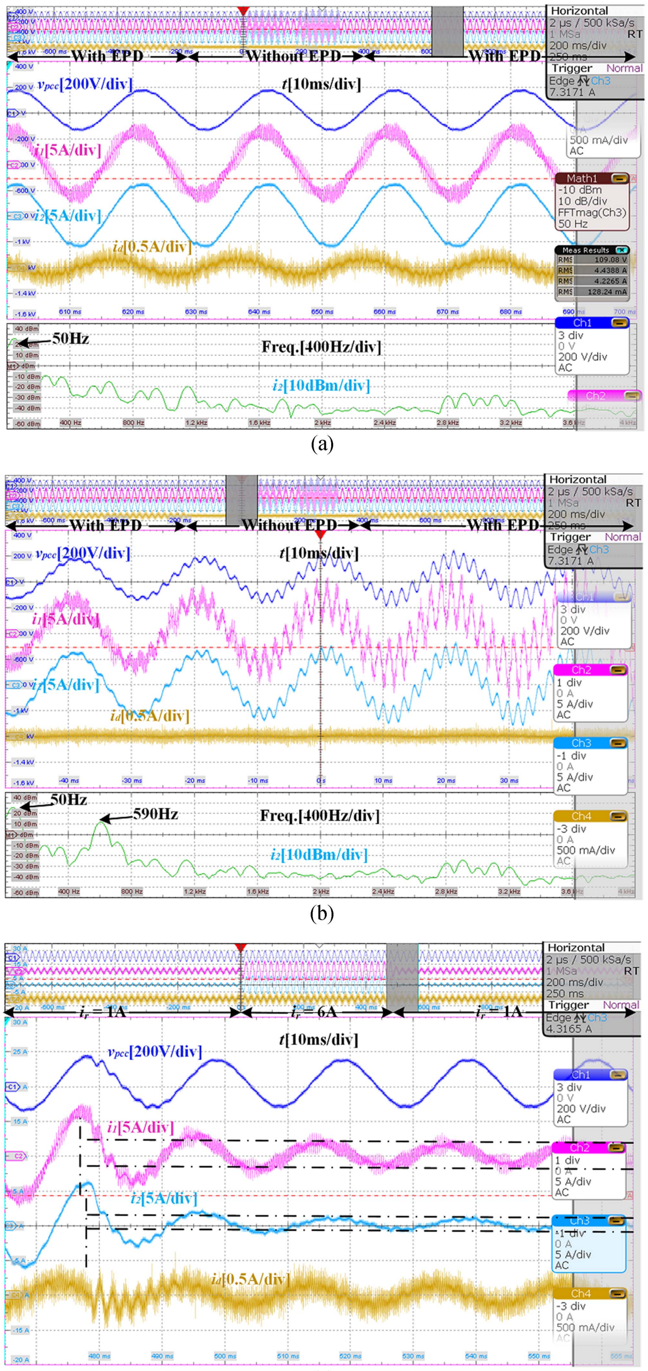

(a)

(b)

(c)

Fig. 13. Experimental waveforms for case II (a) with or (b) without the EPD. (c) Step change of reference current from 6 to 1 A.

B. Simulation Verifications

To validate the proposed method, time-domain simulations are carried out in MATLAB/Simulink for the three cases. The output admittances of the GCI system with and without the EPD for the three cases are measured through the numerical simulations. The measurement procedure is similar to [34]. The results are shown in Fig. 9, where the measured output admittance is all very close to the calculated output admittance. It can be seen in Fig. 9 that the full-frequency passive output

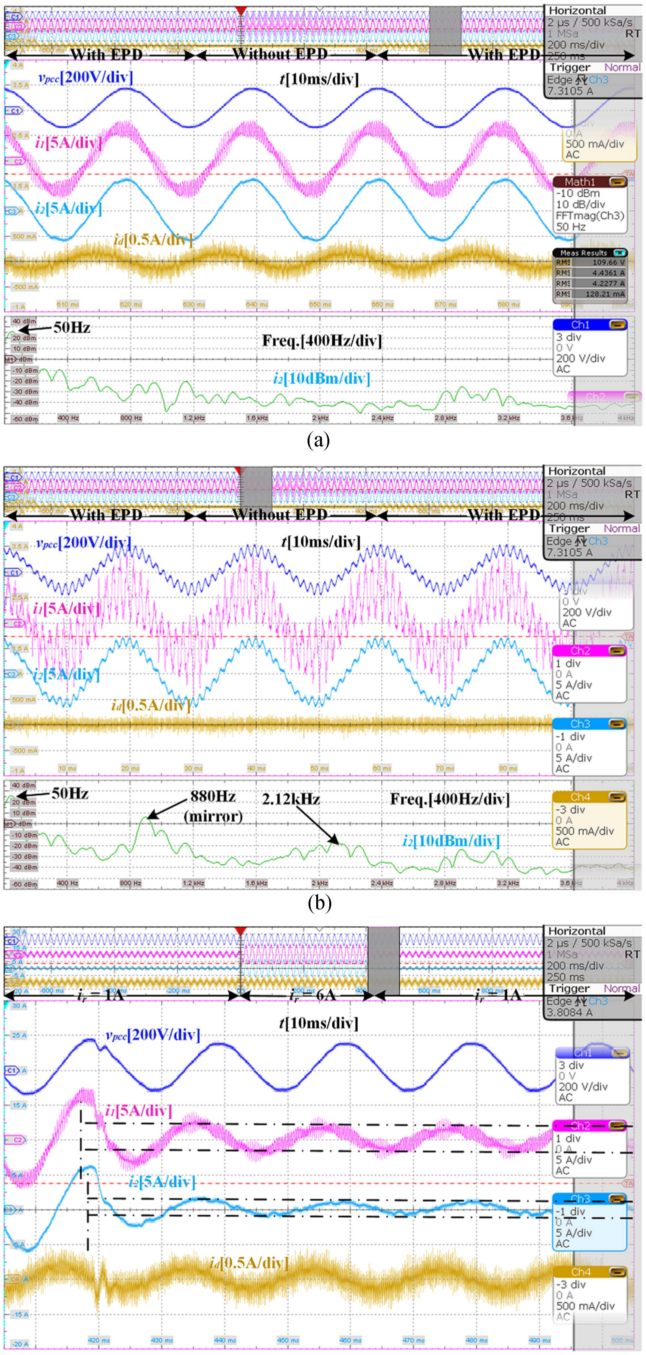

(a)

(b)

(c)

Fig. 14. Experimental waveforms for case III (a) with or (b) without the EPD. (c) Step change of reference current from 6 to 1 A.

admittance of the GCI system can be achieved in the three cases after enabling the EPD, which confirms the correctness of the theoretical analysis.

C. Experimental Verifications

Experiments are performed to further verify the correctness of the theoretical analysis and the effectiveness of the proposed design method. The photo of the experimental setup is shown in Fig. 10, which consists of four three-phase *LCL*-type inverters, one of them is performed as the GCI under test. The control algorithm is implemented on the dSPACE 1005 platform for real-time control. The discretization period of the digital controller is considered the same as the sampling period.

Before conducting experiments, theoretical stability assessments are performed. The interactive stability of the inverter-grid system can be examined by the phase margin (PM) between the intersection of the magnitude response of the output admittance and grid admittance. A PM exceeding 180° indicates instability, while a PM less than 180° indicates stability [1], [23]. Since the use of the EPD can achieve full-frequency passive output admittance, it ensures system interactive stability regardless of the intersection frequency. To verify the effectiveness of the proposed EPD, this article intentionally creates unstable conditions by using a capacitive-type grid. The grid admittance is represented by $Y_g = C_g s + 1/(L_g s)$, where C_g is the power factor correction capacitor and L_g is the grid inductor.

Fig. 11 gives Bode diagrams of $Y_{\rm pcc}$ and Y_g for three different cases. Since the grid impedance is intentionally established, the phase differences at the intersection frequencies, i.e., 2.59 kHz (0.26 p.u.), 522 Hz (0.17 p.u.), and 2.11 kHz (0.70 p.u.), are all over 180°, which indicates the system oscillations.

Fig. 12 gives the experimental waveforms for case I. From Fig. 12(b), it can be observed that the GCI system triggers oscillation when the EPD is disconnected. From the spectrum of i_1, it can be seen that the oscillation frequency is around 2.6 kHz, which is consistent with the theoretical expectation in Fig. 11(a). When the EPD is reconnected [cf., Fig. 12(a)], the GCI system returns to a stable state. The experimental results demonstrate the effectiveness of the proposed EPD in preventing instability for this design case. In addition, the RMS value of i_d is measured as 172.66 mA, and thus, the experimental value of the damping losses is calculated as 0.06 W (4.5×10^{-5} p.u.), which matches the expected value. Fig. 12(c) shows the dynamic performance of the GCI system with the proposed EPD when a step change occurs in the reference current. It takes about a half fundamental period for the output current to track the reference current.

Fig. 13 shows the experimental waveforms for case II. As shown in Fig. 13(b), the GCI system triggers oscillation when the EPD is disabled. From the spectrum of i_2, the oscillation frequency is around 590 Hz, which is in line with the theoretical expectation in Fig. 11(b). The experimental results also validate the effectiveness of the proposed EPD in damping the system oscillation for GCC. Then, the RMS value of i_d is tested at 128.24 mA as shown in Fig. 13(a), and thus the experimental value of the damping losses is calculated as 0.15 W (1.06 × 10-4 p.u.), which also matches the expected value. Fig. 13(c) gives the dynamic performance of the GCI system with the proposed EPD. It takes about one and a half fundamental period for the output current to track the reference current.

Fig. 14 illustrates the experimental waveforms for case III. Oscillation occurs when the EPD is disabled, and there are two oscillation frequencies, i.e., 880 Hz and 2.12 kHz, respectively. Oscillation components around 2.12 kHz comply with the theoretical expectation in Fig. 11(c), and oscillation components around 880 Hz appear due to the well-known folding effect [3]. It demonstrates that resonant frequencies beyond the Nyquist frequency can push the GCI system into instability, as well as the necessity and feasibility of using the proposed EPD to damp these system oscillations. Further, it can be found from Fig. 14(a) that the RMS value of i_d is measured at 128.21 mA, and then the experimental value of the damping losses is calculated as 0.015 W (1.06×10^{-5} p.u.), which matches the expected value. Fig. 14(c) gives the dynamic experimental waveforms, showing a comparable dynamic speed to Case II.

VI. CONCLUSION

In this article, the effect of installation locations of PD on the system efficiency of an *LCL*-type GCI is investigated comprehensively. By leveraging the derived *LCL*-type GCI system model with an IPD or EPD and analyzing their passivity properties of the output admittance seen from the PCC, the EPD addition conditions (EACs) having relaxed passivity compensation burdens for different scenarios are figured out. Then, a general passivity-based EPD design method suitable for EAC-compliant GCIs is put forward to achieve full-frequency passive output admittance. Theoretical analysis and experimental results show that, compared to other state-of-the-art IPD methods, the EPD has sharply reduced the power losses and increased the efficiency when the target system agrees with the EACs, although it fails to cancel out the power loss of PD completely.

In addition, the validities of passivity with EPD in our study cases are only as good as the tolerances for L_1, L_2 and C of the *LCL*-filter are less than 51.5%, 52% and 79% for the HSF-GCI system in single-loop ICC, 10.33%, 11.33% and 98.75% for the LSF-GCI system in single-loop GCC, 24.67%, 20.67% and 30% for the LSF-GCI system in GCC with CCF- and CVF-ADs, respectively.

REFERENCES

[1] C. Wang, X. Wang, Y. He, and X. Ruan, “A passivity-based weighted proportional-derivative feedforward scheme for grid-connected inverters with enhanced harmonic rejection ability,” *IEEE J. Emerg. Sel. Topics Power Electron.*, vol. 11, no. 4, pp. 3656–3668, Aug. 2023.

[2] Z. Lin, X. Ruan, H. Zhang, and L. Wu, “A hybrid-frame control based impedance shaping method to extend the effective damping frequency range of the three-phase adaptive active damper,” *IEEE Trans. Ind. Electron.*, vol. 70, no. 1, pp. 509–521, Jan. 2023.

[3] L. Harnefors, R. Finger, X. Wang, H. Bai, and F. Blaabjerg, “VSC input-admittance modeling and analysis above the nyquist frequency for passivity-based stability assessment,” *IEEE Trans. Ind. Electron.*, vol. 64, no. 8, pp. 6362–6370, Aug. 2017.

[4] V. Pirsto, J. Kukkola, M. Hinkkanen, and L. Harnefors, “Intersample modeling of the converter output admittance,” *IEEE Trans. Ind. Electron.*, vol. 68, no. 11, pp. 11348–11358, Nov. 2021.

[5] J. Zhao, C. Xie, K. Li, J. Zou, and J. M. Guerrero, “Passivity-oriented design of LCL-type grid-connected inverters with luenberger observer-based active damping,” *IEEE Trans. Power Electron.*, vol. 37, no. 3, pp. 2625–2635, Mar. 2022.

[6] X. Wang and F. Blaabjerg, “Harmonic stability in power electronic-based power systems: Concept, modeling, and analysis,” *IEEE Trans. Smart Grid*, vol. 10, no. 3, pp. 2858–2870, May 2019.

[7] I. Z. Petric, P. Mattavelli, and S. Buso, “Passivation of grid-following VSCs: A comparison between active damping and multi-sampled PWM,” *IEEE Trans. Power Electron.*, vol. 37, no. 11, pp. 13205–13216, Nov. 2022.

[8] X. Wang, R. Beres, F. Blaabjerg, and P. C. Loh, “Passivity-based design of passive damping for LCL-filtered voltage source converters,” in *Proc. IEEE Energy Convers. Congr. Expo.*, 2015, pp. 3718–3725.

[9] J. Zhao, C. Xie, and K. Li, “Passivity-based parameter design of passive power filter for the grid-current-controlled VSC,” in *Proc. IEEE Energy Convers. Congr. Expo.*, 2020, pp. 2291–2298.

[10] G. Ma, C. Xie, C. Li, J. Zou, and J. M. Guerrero, “Passivity-based design of passive damping for LCL-type grid-connected inverters to achieve full-frequency passive output admittance,” *IEEE Trans. Power Electron.*, vol. 38, no. 12, pp. 16048–16060, Dec. 2023.

[11] A. Akhavan, H. R. Mohammadi, J. C. Vasquez, and J. M. Guerrero, “Passivity-based design of plug-and-play current-controlled grid-connected inverters,” *IEEE Trans. Power Electron.*, vol. 35, no. 2, pp. 2135–2150, Feb. 2020.

[12] C. Xie, K. Li, J. Zou, and J. M. Guerrero, “Passivity-based stabilization of LCL-type grid-connected inverters via a general admittance model,” *IEEE Trans. Power Electron.*, vol. 35, no. 6, pp. 6636–6648, Jun. 2020.

[13] S. Li and H. Lin, “A capacitor-current-feedback positive active damping control strategy for LCL-type grid-connected inverter to achieve high robustness,” *IEEE Trans. Power Electron.*, vol. 37, no. 6, pp. 6462–6474, Jun. 2022.

[14] S. Li and H. Lin, “Passivity enhancement-based general design of capacitor current active damping for LCL-type grid-tied inverter,” *IEEE Trans. Power Electron.*, vol. 38, no. 7, pp. 8223–8236, Jul. 2023.

[15] D. Pan, X. Ruan, and X. Wang, “Direct realization of digital differentiators in discrete domain for active damping of LCL-type grid-connected inverter,” *IEEE Trans. Power Electron.*, vol. 33, no. 10, pp. 8461–8473, Oct. 2018.

[16] Z. Yang et al., “Wideband dissipativity enhancement for grid-following VSC utilizing capacitor voltage feedforward,” *IEEE J. Emerg. Sel. Topics Power Electron.*, vol. 11, no. 3, pp. 3138–3151, Jun. 2023.

[17] Y. Liu, W. Wu, Y. He, Z. Lin, F. Blaabjerg, and H. S.-H. Chung, “An efficient and robust hybrid damper for LCL- or LLCL-based grid-tied inverter with strong grid-side harmonic voltage effect rejection,” *IEEE Trans. Ind. Electron.*, vol. 63, no. 2, pp. 926–936, Feb. 2016.

[18] J. Ye, A. Shen, Z. Zhang, J. Xu, and F. Wu, “Systematic design of the hybrid damping method for three-phase inverters with high-order filters,” *IEEE Trans. Power Electron.*, vol. 33, no. 6, pp. 4944–4956, Jun. 2018.

[19] H. Liu, L. Li, Y. Liu, D. Xu, and Q. Gao, “Passivity based damping design for grid-connected converter with improved stability,” *IEEE Access*, vol. 7, pp. 185168–185178, 2019.

[20] G. Ma, C. Xie, C. Li, W. Wang, and J. Zou, “Pareto-optimal design of passive damping for megawatt grid-connected inverters,” in *Proc. IEEE 2nd Int. Power Electron. Appl. Symp.*, 2023, pp. 1375–1380.

[21] W. Tang, K. Ma, and Y. Song, “Critical damping ratio to ensure design efficiency and stability of LCL filters,” *IEEE Trans. Power Electron.*, vol. 36, no. 1, pp. 315–325, Jan. 2021.

[22] C. Xie, K. Li, J. Zou, D. Liu, and J. M. Guerrero, “Passivity-based design of grid-side current-controlled LCL-type grid-connected inverters,” *IEEE Trans. Power Electron.*, vol. 35, no. 9, pp. 9813–9823, Sep. 2020.

[23] H. Bai, X. Wang, P. C. Loh, and F. Blaabjerg, “Passivity enhancement of grid-tied converters by series LC-filtered active damper,” *IEEE Trans. Ind. Electron.*, vol. 64, no. 1, pp. 369–379, Jan. 2017.

[24] S. He, D. Zhou, X. Wang, and F. Blaabjerg, “Passivity-based multisampled converter-side current control of LCL-filtered VSCs,” *IEEE Trans. Power Electron.*, vol. 37, no. 11, pp. 13848–13860, Nov. 2022.

[25] Y. Zhao, C. Xie, C. Peng, and J. Zou, “Passivity-based design of frequency adaptive repetitive controller for LCL-type grid-connected inverters,” *IEEE Trans. Power Electron.*, vol. 39, no. 4, pp. 4017–4028, Apr. 2024.

[26] M. Sanatkar-Chayjani and M. Monfared, “Stability analysis and robust design of LCL with multituned traps filter for grid-connected converters,” *IEEE Trans. Ind. Electron.*, vol. 63, no. 11, pp. 6823–6834, Nov. 2016.

[27] C. Xie, K. Li, J. Zou, and D. Liu, “Output admittance passivation for grid-side current controlled LCL-type inverters using capacitor-voltage feedforward,” in *Proc. IEEE Appl. Power Electron. Conf. Expo.*, 2020, pp. 125–130.

[28] C. Wang et al., “Passivity-oriented impedance shaping for LCL-filtered grid-connected inverters,” *IEEE Trans. Ind. Electron.*, vol. 70, no. 9, pp. 9078–9090, Sep. 2023.

[29] *IEEE Standard for Interconnection and Interoperability of Distributed Energy Resources With Associated Electric Power Systems Interfaces*, IEEE Std 1547-2018 (Revision of IEEE Std 1547-2003), Apr. 2018.

[30] M. Sanatkar-Chayjani and M. Monfared, “High-order filter design for high-power voltage-source converters,” *IEEE Trans. Ind. Electron.*, vol. 65, no. 1, pp. 49–58, Jan. 2018.

[31] W. Wu, Y. He, T. Tang, and F. Blaabjerg, “A new design method for the passive damped LCL and LLCL filter-based single-phase grid-tied inverter,” *IEEE Trans. Ind. Electron.*, vol. 60, no. 10, pp. 4339–4350, Oct. 2013.

[32] R. N. Beres, X. Wang, F. Blaabjerg, M. Liserre, and C. L. Bak, “Optimal design of high-order passive-damped filters for grid-connected applications,” *IEEE Trans. Power Electron.*, vol. 31, no. 3, pp. 2083–2098, Mar. 2016.

[33] D. Solatialkaran, F. Zare, T. K. Saha, and R. Sharma, “A novel approach in filter design for grid-connected inverters used in renewable energy systems,” *IEEE Trans. Sustain. Energy*, vol. 11, no. 1, pp. 154–164, Jan. 2020.

[34] C. Xie, D. Liu, K. Li, J. Zou, K. Zhou, and J. M. Guerrero, “Passivity-based design of repetitive controller for LCL-type grid-connected inverters suitable for microgrid applications,” *IEEE Trans. Power Electron.*, vol. 36, no. 2, pp. 2420–2431, Feb. 2021.

Guangda Ma (Student Member, IEEE) received the B.S. degree in electrical engineering from Wenzhou University, Wenzhou, China, in 2020. He is currently working toward the Ph.D. degree in control science and engineering with the School of Automation Engineering, University of Electronic Science and Technology of China, Chengdu, China.

His current research interests include modeling and control of grid-connected inverters for renewable energy generation.

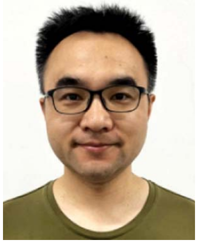

Chuan Xie (Senior Member, IEEE) received the B.S. degree in automation engineering from the University of Electronic Science and Technology of China (UESTC), Chengdu, China, and the Ph.D. degree in power electronics from Zhejiang University (ZJU), Hangzhou, China, in 2007 and 2012, respectively.

Since 2012, he has been a Lecturer with the School of Automation Engineering, UESTC, where he was promoted to an Associate Professor in 2019. Since 2022, he has been a part-time Professor with Shenzhen Institute for Advanced Study at UESTC. From 2015 to 2016, he was a Visiting Scholar with the Department of Energy Technology, Aalborg University. His main research interests include digital control of power electronics, grid synchronization technology, distributed generation systems, microgrids and power quality.

Cheng Li (Student Member, IEEE) received the B.S. and M.S. degrees in automation engineering from the University of Electronic Science and Technology of China, Chengdu, China, in 2020 and 2023, respectively. He is currently working toward the Ph.D. degree in electronic information with the School of Automation Engineering, UESTC.

His current research interests include modeling and control of grid-connected inverters for renewable energy generation.

Chao Peng received the M.S. and Ph.D. degrees in automation from the University of Electronic Science and Technology of China, Chengdu, China, in 2007 and 2012, respectively.

He is currently an Associate Professor with the School of Automation Engineering, Electronic Science and Technology of China, Chengdu. His research interests include renewable power generation system integration and control technologies.

Jianxiao Zou (Member, IEEE) received the B.S., M.S., and Ph.D. degrees in control science and engineering from the University of Electronic Science and Technology of China (UESTC), Chengdu, China in 2000, 2003, and 2009, respectively.

He is currently working as a Professor with UESTC, and has been the Vice Dean with the Shenzhen Institute for Advanced Study, UESTC, since 2020. He was a Visiting Scholar with the University of California, Berkeley, CA, USA, in 2010; and a Senior Visiting Professor with Rutgers, the State University of New Jersey, New Brunswick, NJ, USA, in 2014. His research interests include control theory and control engineering, renewable energy control technologies, and intelligent information processing and control.